

# Skeleton Supervised Airway Segmentation

Mingyue Zhao<sup>1</sup>, Han Li<sup>1</sup>, Li Fan<sup>2</sup>, Shiyuan Liu<sup>2</sup>, Xiaolan Qiu<sup>3</sup>, and S.Kevin Zhou<sup>1</sup>

<sup>1</sup> Center for Medical Imaging, Robotics, Analytical Computing & Learning (MIRACLE), School of Biomedical Engineering, University of Science and Technology of China, Suzhou, China

<sup>2</sup> Department of Radiology, Second Affiliated Hospital, Naval Medical University, Shanghai, China

<sup>3</sup> Suzhou Key Laboratory of Microwave Imaging, Processing and Application Technology Suzhou Aerospace Information Research Institute, Suzhou, China

**Abstract.** Fully-supervised airway segmentation has accomplished significant triumphs over the years in aiding pre-operative diagnosis and intra-operative navigation. However, full voxel-level annotation constitutes a labor-intensive and time-consuming task, often plagued by issues such as missing branches, branch annotation discontinuity, or erroneous edge delineation. label-efficient solutions for airway extraction are rarely explored yet primarily demanding in medical practice. To this end, we introduce a novel skeleton-level annotation (SkA) tailored to the airway, which simplifies the annotation workflow while enhancing annotation consistency and accuracy, preserving the complete topology. Furthermore, we propose a skeleton-supervised learning framework to achieve accurate airway segmentation. Firstly, a dual-stream buffer inference is introduced to realize initial label propagation from SkA, avoiding the collapse of direct learning from SkA. Then, we construct a geometry-aware dual-path propagation framework (GDP) to further promote complementary propagation learning, composed of hard geometry-aware propagation learning and soft geometry-aware propagation guidance. Experiments reveal that our proposed framework outperforms the competing methods with SKA, which amounts to only 1.96% airways, and achieves comparable performance with the baseline model that is fully supervised with 100% airways, demonstrating its significant potential in achieving label-efficient segmentation for other tubular structures, such as vessels.

**Keywords:** Airway segmentation · Skeleton supervised learning · Geometry-aware dual-path propagation learning.

## 1 Introduction

Airway segmentation is fundamentally important for early diagnosis, treatment, and ongoing assessment of lung diseases [1, 2]. Recently, deep learning-based algorithms [3–11] have emerged as highly effective tools for extracting airways. Despite this, existing algorithms still face significant challenges in obtaining high-quality voxel-level annotations for the airway, mainly attributed to the inherent

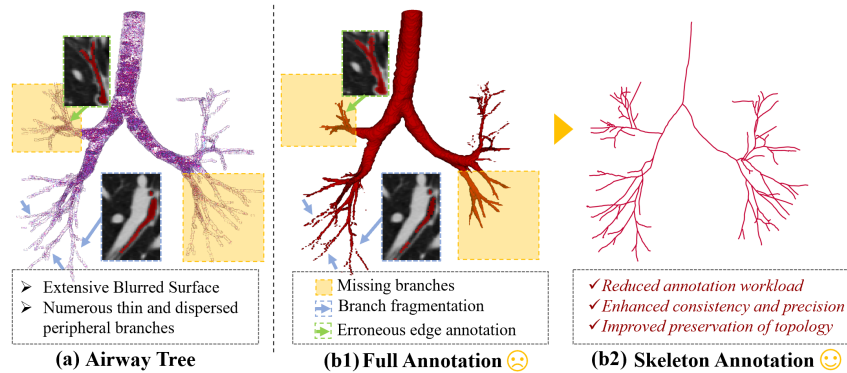


**Fig. 1. Motivation** for introducing the skeleton level annotation for the airway.

characteristics of airway tree: 1) *Extensive Blurred Surface/Edge Area*. The airway tree necessitates labeling more edge voxels that gradually blur along the depth of the airway. 2) *Numerous thin and dispersed peripheral branches*. These branches occupy a significant proportion and exhibit diverse directions, necessitating annotators to constantly adjust their observation perspectives. These two factors make voxel-wise annotation a time-consuming and labor-intensive task. Furthermore, compared to the labeling of near-convex structures such as organs or tumors, it inevitably leads to more inconsistent and noisy annotations, such as missing branches, branch fragmentation, or erroneous edge annotations (as shown in Fig. 1). Hence, there is an urgent need to propose a label-efficient solution for bronchioles segmentation.

Partial annotation learning [12–25] utilizing only a subset of annotated pixels has demonstrated comparable performance to fully supervised learning both in natural images and medical images. It shows great potential in difficult-to-annotate segmentation tasks, yet its application in tubular structures remains unexplored. Xu *et al.* [18] propose a partial supervision manner for vessel segmentation with only a few 2D patches annotated. Zhang *et al.* [17] achieve weakly supervised learning of coronary artery vessel segmentation by randomly selecting partial vessel branches for voxel-level annotation. Despite significantly alleviating the annotation burden compared with the full voxel-level annotation, they still adopt the voxel-wise annotation fashion while paying little attention to topological completeness. The challenge of elaborately delineating fine, dispersed branches of the airway tree remains. To this end, we introduce a novel Skeleton Annotation (SkA) tailored to the airway.

As illustrated in Fig. 1, the SkA shows three main superiority over the voxel-level annotations: 1) **Reduced annotation workload**. SkA, focusing only on the skeleton, is simpler and more efficient than voxel-level labeling, which only needs to annotate 1.96% of the airway voxels (save 80+% time) and reduce numerous blurred edge annotations. 2) **Enhanced annotation consistency and precision**. Voxels annotated in SKA tend to be closer to the lumen center, ex-

hibiting more prominent airway characteristics, which effectively enhances the accuracy and consistency of annotations. 3) **Improved preservation of topology**. This method is more conducive to maintaining the complete topological structure of the airway, which is vital for accurate modeling and analysis.

Nevertheless, relying solely on SkA to achieve reliable voxel-wise airway prediction still poses significant challenges: 1) *Extremely sparse supervision*: Since only the skeleton is annotated, the supervision signal is too sparse to support the training of the network. 2) *Limited diversity in supervision signals*: This issue can be observed in two main aspects. The first is the absence of edge annotations, which is crucial for defining precise boundaries in segmentation tasks. Secondly, due to the inherent nature of SkA, this labeling method exhibits a stronger preference [26] for annotation positions (i.e., closer to the lumen center) compared to other sparse annotations (e.g., scribbles) that can cover a broader area with an accumulation of extensive annotated samples. This limited annotation bias implies less effective information, leading to impracticality in direct training.

To address this, we further propose a novel skeleton-supervised learning method for airway segmentation. Firstly, it employs a dual-stream buffer inference strategy to propagate knowledge from SkA to unannotated regions, avoiding the collapse of learning directly from skeleton-level annotation. Secondly, considering the tree-like structure, geometry-aware dual-path propagation learning, composed of hard geometry-aware learning and soft geometry-aware guidance, is constructed to achieve accurate airway segmentation.

The main contributions are summarized as follows. **1)** To the best of our knowledge, we are the first to introduce skeleton-level annotation (SkA) into airway segmentation. It significantly reduces annotation burden while enhancing annotation consistency and preserving more complete topology, aligning more closely with the characteristics of tubular structures. **2)** Tailored for airway segmentation, a skeleton-supervised learning method is proposed. Firstly, considering both the spatial locations and grayscale information of SkA, initial label propagation from SkA is conducted utilizing a dual-stream buffer inference strategy (DBI), avoiding the collapse of learning directly from SkA. Secondly, considering the tree-like structure, a geometry-aware dual-path propagation learning method, composed of hard geometry-aware learning and soft geometry-aware guidance, is presented in a dual-supervision manner to further achieve complementary label propagation learning. **3)** Extensive experiments indicate that our method achieves comparable performance to the fully-supervised method with only **1.96%** annotated voxels. Moreover, our method exhibits greater potential for diverse tubular structure segmentation tasks.

## 2 Methodology

Given a CT volume  $X$  with the corresponding SkA  $Y_s$ , we aim to learn a mapping  $\mathcal{F} : X \mapsto \hat{Y}$  based on SkA, where  $\hat{Y}$  is the voxel-level airway prediction. As shown in Fig. 2, there are two stages in our methods: 1) Label Propagation from Skeleton Annotations and 2) Geometry-aware Dual-path Propagation Learning.

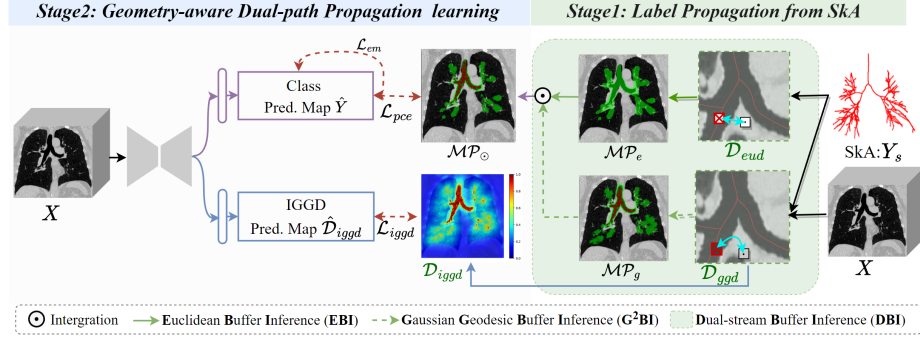


**Fig. 2.** Overview of our skeleton-supervised airway segmentation framework.  $MP_g$ ,  $MP_e$  and  $MP_\odot$  are the mask proposals after  $G^2BI$ , EBI, and DBI, where red, green denotes foreground and unknown regions, the rest area is the background.

**Label Propagation from Skeleton Annotations.** We propose an effective label propagation method, named Dual-stream Buffer Inference (DBI), to propagate the knowledge from SKA to more unlabeled voxels. As shown in Fig. 2, it includes two modules:

Gaussian Geodesic distance Buffer Inference ( $G^2BI$ ). Specifically, given a point  $i$  in image space  $\Omega$ ,  $\Omega_s = \{i | Y_s(i) = 1\}$  denotes the initial annotated voxel set in SKA. Geodesic distance [27] considers the pixels' spatial distance relationship and their appearance similarity, making it better suited to the airway with severe intra-scale imbalance. However, the geodesic distance-based label propagation relies on a strong prerequisite: intra-class pixels have similar grayscale values and show flat gradients. To improve the label consistency within homogeneous areas, Gaussian smoothing is implemented on images before applying the geodesic distance transformation. Concretely, for each voxel  $i \in \Omega$ , the Gaussian geodesic distance from  $i$  to  $\Omega_s$  can be formulated as:

$$\mathcal{D}_{ggd}[i, \Omega_s, g_\sigma(x)] = \min_{j \in \Omega_s} \mathcal{D}_{ged}[i, j, g_\sigma(x)], \quad (1)$$

$$\mathcal{D}_{ged}[i, j, g_\sigma(x)] = \min_{p \in \mathcal{P}_{i \rightarrow j}, j \in \Omega_s} \int_0^1 \|\nabla g_\sigma(x)(p(\xi)) \cdot \mathbf{u}(\xi)\| d\xi, \quad (2)$$

where  $g_\sigma(\cdot)$  denotes a Gaussian filter function with a standard deviation of  $\sigma$ .  $\mathcal{P}_{i \rightarrow j}$  is the set of all possible paths from  $i$  to  $j$  for  $j \in \Omega_s$ ,  $p \in \mathcal{P}_{i \rightarrow j}$  is one feasible path and parameterized by  $\xi \in [0, 1]$ .  $\mathbf{u}$  is a unit vector tangent to the direction of path  $p$ . The calculated  $\mathcal{D}_{ggd}[i, j, g_\sigma(x)]$  is visualized in Fig. 3(c1).

To facilitate the label expansion of the foreground and background, we exploit bilateral  $G^2BI$ . Let  $\Omega_{f_1}$  and  $\Omega_{b_1}$  denote the foreground and background after label propagation respectively, then they can be obtained by:

$$\Omega_{f_1} = \{i | i \in \Omega \text{ and } \mathcal{D}_{ggd}(i) < \delta_1 \max(\mathcal{D}_{ggd})\}, \quad (3)$$

$$\Omega_{b_1} = \{i | i \in \Omega \text{ and } \mathcal{D}_{ggd}(i) > \delta_2 \max(\mathcal{D}_{ggd})\}, \quad (4)$$

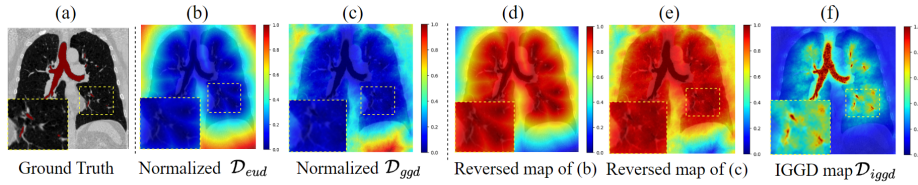


**Fig. 3.** Visualization of distance maps. (d) and (e), as the reversed maps of (b) and (c), are used for better visual contrast. The  $\mathcal{D}_{iggd}$  (f) is much clearer than (d) and (e).

where  $\delta_1, \delta_2 \in [0, 1]$  are hyper-parameters indicating the degree of expansion and  $\delta_1 < \delta_2$ . The mask proposal  $\mathcal{MP}_g$  generated from G<sup>2</sup>BI, is depicted in Fig. 2.

Euclidean distance Buffer Inference (EBI). The Euclidean distance, as an absolute spatial distance metric, is employed as an additional constraint for label expansion. In light of the pronounced intra-class scale imbalance within the airway tree, where the narrowest branches may measure only one pixel in width, Euclidean distance fails to achieve reliable diffusion of foreground skeleton labels. Consequently, we implement unilateral EBI to achieve background expansion:

$$\Omega_{b_2} = \{i | i \in \Omega - \Omega_s \text{ and } \mathcal{D}_{eud}(i) > \gamma \max(\mathcal{D}_{eud})\}, \quad (5)$$

where  $\mathcal{D}_{eud}(i) = \min_{j \in \Omega_s} \|i - j\|_2$  and  $\gamma \in [0, 1]$  is a hyper-parameter to control the degree of background expansion. Similarly,  $\mathcal{MP}_e$ , depicted in Fig. 2, denote the generated mask proposal after EBI.

Thus far, the foreground and background after propagation can be represented as  $\Omega_B = \Omega_{b_1} \cup \Omega_{b_2}$  and  $\Omega_F = \Omega_{f_1}$ , respectively. Fig. 2 gives an example of final mask proposal  $\mathcal{MP}_\odot$ . For simplicity, we denote the set of labeled voxels as  $\Omega_L = \Omega_B \cup \Omega_F$  and the voxel set with unknown labels as  $\Omega_U = \Omega - \Omega_L$ .

**Geometry-aware Dual-path Propagation Learning.** As illustrated in Fig. 2, we devise a dual-path network in a multi-head manner to achieve skeleton-supervised learning. The main branch is dedicated to voxel-wise airway prediction, supervised by the proposal masks  $\mathcal{MP}_\odot$  (acting as hard geometry-aware information). The Inverse Gaussian Geodesic Distance map (IGGD) serves as fine-grained soft geometry-aware information in the auxiliary branch to aid the training of the main branch.

Hard Geometry-Aware Propagation Learning. Similarly to [13, 15, 16, 28], we impose the partial cross-entropy loss solely on the annotated pixels ( $i \in \Omega_L$ ):

$$\mathcal{L}_{pce} = -\frac{1}{|\Omega_L|} \sum_{i \in \Omega_L} (\hat{Y}(i) \log(\mathcal{MP}_\odot(i)) + (1 - \hat{Y}(i)) \log(1 - \mathcal{MP}_\odot(i))). \quad (6)$$

Besides, to encourage the model to produce high-confidence predictions for unannotated voxels, entropy minimization [29] is applied to the class probability prediction maps, with the corresponding supervised loss formulated as:

$$\mathcal{L}_{em} = -\frac{1}{|\Omega_U|} \sum_{i \in \Omega_U} \mathcal{MP}_\odot(i) \log(\mathcal{MP}_\odot(i)). \quad (7)$$

Soft Geometry-Aware Propagation Guidance. Despite that initial label propagation for SkA partially alleviates the problem of sparse supervision, the model still lacks the fine-grained structural perception of the airway. We find that the Gaussian geodesic distance map  $\mathcal{D}_{ggd}$  implicitly incorporates more fine-grained multiscale-aware and edge-aware information, which is well-suited as geometry-aware information to boost voxel-wise predictions in the main segmentation branch. Considering the similarity in grayscale between lung parenchyma and airways, we perform an inverse transformation on  $\mathcal{D}_{ggd}$  to get the IGGD maps:  $\mathcal{D}_{iggd}(i) = \mathbf{1}/(\mathcal{D}_{ggd}(i) + c)$ , accentuating inter-class difference while avoiding over-segmentation. Where  $c = 1$  to ensure  $\mathcal{D}_{iggd} \in [0, 1]$  while avoiding division by zero. Compared with (e) and (f) in Fig. 3, the inverse transformation significantly enhances the airway branches within lung, thereby providing fine-grained and robust auxiliary information for branch segmentation. Mean Squared Error (MSE) loss is adopted in this branch:

$$\mathcal{L}_{iggd} = \frac{1}{N} \sum_{i=1}^N (\hat{\mathcal{D}}_{iggd} - \mathcal{D}_{iggd})^2, \quad (8)$$

where  $\hat{\mathcal{D}}_{iggd}$  represents the prediction map of the auxiliary branch. Finally, the proposed skeleton-supervised learning framework can be trained by minimizing:  $\mathcal{L}_{total} = \mathcal{L}_{pce} + \lambda_1 \mathcal{L}_{em} + \lambda_2 \mathcal{L}_{iggd}$ , where  $\lambda_1$  and  $\lambda_2$  are the trade-off weights. Thus far, the mask proposals generated from DBI serve as hard geometry-aware information, providing local absolute supervision guidance for segmentation networks. While the IGGD map as soft geometry-aware information, offers global fine-grained scale-aware and edge-aware guidance for segmentation.

### 3 Experiment and Results

**Datasets and Evaluation Metrics.** Experiments are implemented on the public Binary Airway Segmentation (BAS) Dataset [3], consisting of 90 CT scans. ATM22 [30] dataset consisting of 299 CT scans, is introduced as external validation. SkA of BAS dataset is first extracted using MIMICs software and then manually corrected by a panel of well-trained experts [31]. Following [4, 6, 8, 32], we adopt volumetric-based metrics (Dice Similarity Coefficient (DSC), True Positive Rate (TPR), and False Positive Rate (FPR)) and topology-based metrics (Branches Detected (BD) [32], Branches Detected (BD\*) [4], Tree-length Detected (TD) [32]) for evaluation. BD and BD\* represent cases where a branch is regarded as detected when 80% or just one voxel of it is detected. Only the largest component of segmentation results are evaluated and five-fold cross-validation is conducted to obtain the final results. The source code will be available.

**Comparative Test.** In Table 1, we compare our approach with other sparse-supervised learning methods, including regularization learning [28, 29, 37] and dynamic pseudo-label learning [35, 36]. Note that some of the methods (marked by †) utilize our mask proposal  $\mathcal{MP}_{\odot}$  during training instead of the SkA, thus avoiding the crash of direct learning. Results demonstrate that **1)** our method

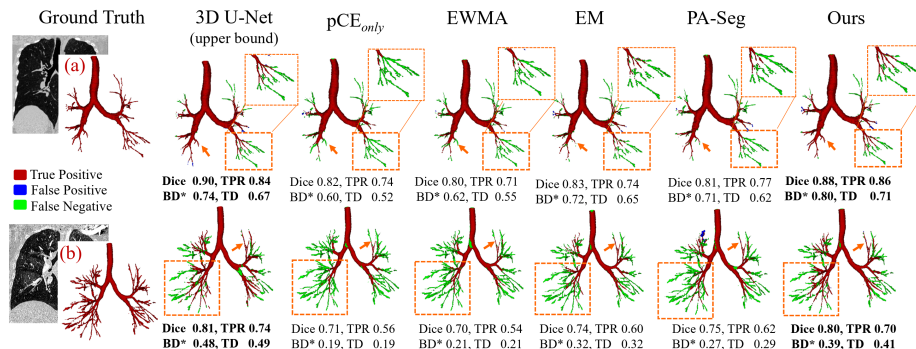


Fig. 4. Segmentation results on a moderate case (a) and a challenging case (b). Orange boxes and arrows highlight the branches with significant segmentation discrepancies.

Table 1. Quantitative results based on BAS [3] and ATM22 dataset [30].

Train Data	Test Data	Annotation	Methods	DSC(%) <sup>↑</sup>	TPR(%) <sup>↑</sup>	FPR(%) <sup>↓</sup>	BD(%) <sup>↑</sup>	BD*(%) <sup>↑</sup>	TD(%) <sup>↑</sup>
BAS	BAS	FA	U-Net [33](Upper bound)	90.53±0.4	91.13±0.7	.032±0.007	62.75±2.4	79.52±1.1	75.10±1.6
			pCE <sub>only</sub> [34] <sup>†</sup>	86.21±0.3	78.99±0.7	.010±.004	40.70±2.9	60.21±3.3	53.06±3.4
		EWMA [35] <sup>†</sup>	84.77±0.3	77.21±0.1	.012±.001	41.25±0.1	61.26±0.1	54.48±0.2	
		Luo <i>et al.</i> [36] <sup>†</sup>	84.74±0.3	77.20±0.1	.010±.001	41.18±0.1	61.33±0.1	54.60±0.3	
		Gatedcrf [37] <sup>†</sup>	84.92±0.7	79.84±2.6	.025±.010	45.93±2.5	65.35±2.3	58.55±2.5	
		PA-Seg [28]	85.45±0.1	81.05±0.7	.030±.005	48.55±0.6	67.43±0.4	61.13±0.8	
		EM [29] <sup>†</sup>	87.62±0.6	81.20±0.7	.010±.001	51.64±1.3	69.69±1.2	63.93±1.4	
	Ours	<b>88.79±0.3</b>	<b>87.60±0.8</b>	<b>.030±.001</b>	<b>58.65 ± 1.1</b>	<b>75.82 ± 1.1</b>	<b>70.55 ± 1.0</b>		
	ATM22	FA	U-Net [33]	91.29±0.2	89.88±0.5	.021±.001	55.93 ± 0.8	80.07 ± 0.5	71.68 ± 0.6
		SkA	Ours	89.60±0.1	86.82±0.5	.021±.001	52.66 ± 0.4	76.64 ± 0.7	67.31 ± 0.5

achieves superior performance, outperforming the 2nd approach [29] with considerable margins (+6.4% TPR, +7.0% BD, +6.1% BD\*, +3.6% TD). We argue that the regularization learning and dynamic pseudo-label learning approaches emphasize learning a more confident and robust segmentation, which hinders the network from achieving better recall for high-frequency details (such as airway edges or fine peripheral branches). **2)** Our method achieves segmentation performance close to fully supervised learning with only 1.96% voxel annotations. **3)** Additional **Cross-dataset validation** (i.e., train on BAS, test on ATM22) also confirms the strong generalization ability of our algorithm.

**Ablation Study.** Ablation study is provided in Table 2 to evaluate the importance of the two key designs: 1) label propagation from SkA (i.e., the DBI strategy) and 2) GDP framework. From **1)**, we observe that the initial label propagation strategy and parameter tuning significantly impact the model’s performance. Particularly, i) the Gaussian smoothing ( $GBI \rightarrow G^2BI$ ) contributes a substantial improvement of 9.77% in DSC and 16.95% in TD, primarily attributed to the enhanced consistency within labels, thereby enabling the reliable label propagation. ii) the degree of airway label expansion (i.e., the selection of  $\delta 1$ ) has a greater influence. A smaller extent implies less but more accurate airway label diffusion, while a larger extent implies more but noisier label diffusion, thus facing higher risks of false positives. Additional visual comparisons of various label propagation strategies and parameter selections can be found in

**Table 2.** Results of ablation study. *GBI* denotes Geodesic distance-based buffer inference without Gaussian smoothing. The gray shading indicates our final settings for each group of ablation experiments.

1) Ablation for DBI strategy ( $\mathcal{L} = \mathcal{L}_{pcc}$ for default, and $DBI = EBI + G^2BI$ )										
Setting		Params.		Metrics						
<i>GBI</i>	<i>G<sup>2</sup>BI</i>	<i>DBI</i>	$\delta_1$	$\delta_2$	DSC(%) $\uparrow$	TPR(%) $\uparrow$	FPR(%) $\downarrow$	BD(%) $\uparrow$	BD*(%) $\uparrow$	TD(%) $\uparrow$
(a)	✓	✓	0.01	0.07	75.91 $\pm$ 0.7	77.66 $\pm$ 1.4	.280 $\pm$ .059	24.34 $\pm$ 2.2	37.39 $\pm$ 3.7	33.59 $\pm$ 2.9
			0.01	0.07	85.68 $\pm$ 0.9	78.70 $\pm$ 1.3	.009 $\pm$ .002	38.69 $\pm$ 1.3	57.63 $\pm$ 1.6	50.54 $\pm$ 1.5
(b)	✓	✓	0.005	0.07	83.30 $\pm$ 0.4	73.24 $\pm$ 0.9	.004 $\pm$ .002	36.89 $\pm$ 5.3	55.75 $\pm$ 6.9	49.08 $\pm$ 6.7
			0.02	0.07	72.25 $\pm$ 2.3	85.40 $\pm$ 1.6	.250 $\pm$ .047	53.74 $\pm$ 4.3	71.42 $\pm$ 3.7	65.00 $\pm$ 4.1
			0.01	0.06	82.94 $\pm$ 0.5	74.97 $\pm$ 0.3	.020 $\pm$ .001	39.90 $\pm$ 0.8	59.28 $\pm$ 1.0	52.48 $\pm$ 1.0
			0.01	0.08	81.20 $\pm$ 3.1	78.85 $\pm$ 2.0	.060 $\pm$ .018	41.62 $\pm$ 1.6	60.58 $\pm$ 2.1	53.58 $\pm$ 1.8
			0.01	0.07	86.21 $\pm$ 0.3	78.99 $\pm$ 0.7	.010 $\pm$ .004	40.70 $\pm$ 2.9	60.21 $\pm$ 3.3	53.06 $\pm$ 3.4
2) Ablation for GDP framework ( $DBI = EBI + G^2BI$ for default)										
$\mathcal{L}_{pcc}$	$\mathcal{L}_{em}$	$\mathcal{L}_{iggd}$	$\lambda_1$	$\lambda_2$	DSC(%) $\uparrow$	TPR(%) $\uparrow$	FPR(%) $\downarrow$	BD(%) $\uparrow$	BD*(%) $\uparrow$	TD(%) $\uparrow$
(c)	✓	✓	1.5	20	86.21 $\pm$ 0.3	78.99 $\pm$ 0.7	.010 $\pm$ .004	40.70 $\pm$ 2.9	60.21 $\pm$ 3.3	53.06 $\pm$ 3.4
			1.5	20	87.62 $\pm$ 0.6	81.20 $\pm$ 0.7	.010 $\pm$ .001	51.64 $\pm$ 1.3	69.69 $\pm$ 1.2	63.93 $\pm$ 1.4
			1.5	20	88.79 $\pm$ 0.3	87.60 $\pm$ 0.8	.030 $\pm$ .001	58.65 $\pm$ 1.1	75.82 $\pm$ 1.1	70.55 $\pm$ 1.0
(d)	✓	✓	1	20	87.82 $\pm$ 1.1	86.50 $\pm$ 1.1	.030 $\pm$ .001	58.98 $\pm$ 1.4	75.39 $\pm$ 1.0	70.23 $\pm$ 1.2
			2	20	87.50 $\pm$ 0.9	85.36 $\pm$ 2.7	.030 $\pm$ .001	56.04 $\pm$ 3.5	73.35 $\pm$ 3.7	67.84 $\pm$ 3.5
			1.5	10	88.19 $\pm$ 0.3	85.90 $\pm$ 0.8	.030 $\pm$ .001	55.62 $\pm$ 1.8	72.28 $\pm$ 1.5	67.27 $\pm$ 1.5
			1.5	40	88.75 $\pm$ 0.4	86.77 $\pm$ 1.0	.030 $\pm$ .001	56.13 $\pm$ 0.8	73.81 $\pm$ 0.6	68.35 $\pm$ 0.7

the Suppl. Material. Besides, **2)** the ablation study of GDP confirms that the addition of entropy minimization regularization loss and IGGD prediction loss significantly improved segmentation performance. The former strengthens the model’s predictive capability for labeled regions in mask proposals (manifested in better topological-level metrics), but has limited performance improvement in uncertain regions (manifested in limited TPR improvement). IGGD, as soft geometry-aware information, provides the model with more scale and edge perception, resulting in significant performance improvements at both topological and voxel levels (+6.4% TPR and +7.0% BD).

**Qualitative Results.** Fig. 4 gives an intuitive performance comparison for the above methods on both a moderate case (a) and a challenging case (b). It can be observed that our method maintains less false positive detection even in noisy images, while detecting more distal branches compared to other methods. Additionally, we achieve comparable performance with the fully supervised method and even superior topological metrics in some cases.

## 4 Conclusion

Tailored to label-effective airway segmentation, we introduce a novel skeleton annotation strategy, which alleviates the annotation burden, preserves complete topology, and enhances annotation consistency and accuracy. Based on that, we further propose a skeleton-supervised learning method. To address the extremely sparse supervision challenge, a dual-stream buffer inference strategy is first proposed to realize initial label propagation. Then, a geometry-aware dual-path



propagation learning method is presented in a dual-supervision manner to further achieve complementary label propagation learning. Our proposed method achieved excellent airway segmentation performance with only 1.96% annotated voxels, approaching the fully supervised performance. This shows great potential for generalization to more tubular structure segmentation tasks.

## References

1. D. Jong et al. Airway management for covid-19: a move towards universal video-laryngoscope? *The Lancet Respiratory Medicine*, 8(6):555, 2020.
2. D. Xiao et al. Prevalence and risk factors of small airway dysfunction, and association with smoking, in china: findings from a national cross-sectional study. *The Lancet Respiratory Medicine*, 8(11):1081–1093, 2020.
3. Y. Qin et al. AirwayNet-SE: A Simple-Yet-Effective Approach to Improve Airway Segmentation Using Context Scale Fusion. In *IEEE ISBI*, pages 809–813, Iowa City, IA, USA, April 2020. IEEE.
4. Y. Qin et al. Learning Tubule-Sensitive CNNs for Pulmonary Airway and Artery-Vein Segmentation in CT. *IEEE TMI*, 40(6):1603–1617, June 2021.
5. W. Yu et al. Break: Bronchi Reconstruction by Geodesic Transformation and Skeleton Embedding. In *IEEE ISBI*, pages 1–5, Kolkata, India, March 2022. IEEE.
6. H. Zheng et al. Alleviating Class-Wise Gradient Imbalance for Pulmonary Airway Segmentation. *IEEE TMI*, 40(9):2452–2462, September 2021.
7. A. Wang et al. NaviAirway: a Bronchiole-sensitive Deep Learning-based Airway Segmentation Pipeline, June 2022.
8. H. Zheng et al. Refined Local-imbalance-based Weight for Airway Segmentation in CT. In Marleen de Bruijne, Philippe C. Cattin, Stéphane Cotin, Nicolas Padoy, Stefanie Speidel, Yefeng Zheng, and Caroline Essert, editors, *MICCAI*, volume 12901, pages 410–419. Springer International Publishing, Cham, 2021. Series Title: Lecture Notes in Computer Science.
9. M. Zhang et al. Towards connectivity-aware pulmonary airway segmentation. *IEEE JBHI*, 2023.
10. M. Zhang et al. Fda: Feature decomposition and aggregation for robust airway segmentation. In *MICCAI*, pages 25–34. Springer, 2021.
11. T. Zhao et al. Bronchus segmentation and classification by neural networks and linear programming. In *MICCAI*, pages 230–239. Springer, 2019.
12. K. Zhang et al. Shapepu: A new pu learning framework regularized by global consistency for scribble supervised cardiac segmentation. In *MICCAI*, pages 162–172. Springer, 2022.
13. Q. Chen et al. Scribble2d5: Weakly-supervised volumetric image segmentation via scribble annotations. In *MICCAI*, pages 234–243. Springer, 2022.
14. J. Lee et al. Weakly supervised segmentation of small buildings with point labels. In *ICCV*, pages 7406–7415, 2021.
15. Y. Wei et al. Scribble-based weakly supervised deep learning for road surface extraction from remote sensing images. *IEEE Transactions on Geoscience and Remote Sensing*, 60:1–12, 2021.
16. M. Zhou et al. Weakly supervised medical image segmentation via superpixel-guided scribble walking and class-wise contrastive regularization. In *MICCAI*, pages 137–147. Springer, 2023.

17. Z. Zhang et al. Partial vessels annotation-based coronary artery segmentation with self-training and prototype learning. In *MICCAI*, pages 297–306. Springer, 2023.
18. Y. Xu et al. Partially-supervised learning for vessel segmentation in ocular images. In *MICCAI*, pages 271–281. Springer, 2021.
19. M. Han et al. Scribble-based 3d multiple abdominal organ segmentation via triple-branch multi-dilated network with pixel-and class-wise consistency. In *MICCAI*, pages 33–42. Springer, 2023.
20. H. Cai et al. 3d medical image segmentation with sparse annotation via cross-teaching between 3d and 2d networks. In *MICCAI*, pages 614–624. Springer, 2023.
21. A. Wang et al. S<sup>2</sup>me: Spatial-spectral mutual teaching and ensemble learning for scribble-supervised polyp segmentation. In *MICCAI*, pages 35–45, Cham, 2023. Springer Nature Switzerland.
22. H. Li et al. Segment membranes and nuclei from histopathological images via nuclei point-level supervision. In *MICCAI*, pages 539–548. Springer, 2023.
23. K. Zhang et al. Cyclemix: A holistic strategy for medical image segmentation from scribble supervision. In *CVPR*, pages 11656–11665, 2022.
24. S. Li et al. Pln: Parasitic-like network for barely supervised medical image segmentation. *IEEE TMI*, 42(3):582–593, 2022.
25. C. Zhou et al. Progressive bayesian inference for scribble-supervised semantic segmentation. In *AAAI*, volume 37, pages 3751–3759, 2023.
26. Y. Wang et al. Blpseg: Balance the label preference in scribble-supervised semantic segmentation. *IEEE TIP*, 2023.
27. G. Wang et al. Deepigeos: a deep interactive geodesic framework for medical image segmentation. *IEEE TPAMI*, 41(7):1559–1572, 2018.
28. S. Zhai et al. Pa-seg: Learning from point annotations for 3d medical image segmentation using contextual regularization and cross knowledge distillation. *IEEE TMI*, 2023.
29. Y. Grandvalet et al. Semi-supervised learning by entropy minimization. *Advances in neural information processing systems*, 17, 2004.
30. M. Zhang et al. Multi-site, multi-domain airway tree modeling. *Medical Image Analysis*, 90:102957, 2023.
31. M. Zhao et al. Gdds: Pulmonary bronchioles segmentation with group deep dense supervision. *arXiv preprint arXiv:2303.09212*, 2023.
32. P. Lo et al. Extraction of Airways From CT (EXACT’09). *IEEE TMI*, 31(11):2093–2107, November 2012.
33. Özgün. Çiçek et al. 3d u-net: Learning dense volumetric segmentation from sparse annotation. In *MICCAI*, pages 424–432, Cham, 2016. Springer International Publishing.
34. D. Lin et al. Scribblesup: Scribble-supervised convolutional networks for semantic segmentation. In *CVPR*, pages 3159–3167, 2016.
35. H. Lee et al. Scribble2label: Scribble-supervised cell segmentation via self-generating pseudo-labels with consistency. In *MICCAI*, pages 14–23. Springer, 2020.
36. X. Luo et al. Scribble-supervised medical image segmentation via dual-branch network and dynamically mixed pseudo labels supervision. In *MICCAI*, pages 528–538. Springer, 2022.
37. M. Tang et al. On regularized losses for weakly-supervised cnn segmentation. In *ECCV*, pages 507–522, 2018.